Published in final edited form as:
Nanoscale. 2017 January 26; 9(4): 1434–1442. doi:10.1039/c6nr07894j.

Mesoporous carbon nanoshells for high hydrophobic drug loading, multimodal optical imaging, controlled drug release, and synergistic therapy

Hui Wang[#a], **Kui Wang**[#a], **Qingxin Mu**[a], **Zachary R. Stephen**[a], **Yanyan Yu**[b], **Shuiqin Zhou**[b], and **Miqin Zhang**[a]

[a] Department of Materials Science and Engineering, University of Washington, Seattle, Washington 98195, United States

[b] Department of Chemistry of The College of Staten Island and The Graduate Center, The City University of New York, Staten Island, New York 10314, United States

[#] These authors contributed equally to this work.

Abstract

Loading and controlled release of sufficient hydrophobic drugs to tumor cells has been the bottleneck in chemotherapy for decades. Here we report the development of a fluorescent and mesoporous carbon nanoshell (FMP-CNS) that exhibits a loading capacity for hydrophobic drug paclitaxel (PTX) as high as ~80 wt% and releases drug in a controllable fashion under NIR irradiation (825 nm) at a intensity of 1.5 W/cm^2. The high drug loading is primarily attributed to its mesoporous structure and to the supramolecular π-stacking between FMP-CNSs and PTX molecules. The FMP-CNS also exhibits wavelength-tunable and upconverted fluorescent property and thus can serve as an optical marker for confocal, two-photon, and near infrared (NIR) fluorescence imaging. Further, our *in vitro* results indicate that FMP-CNSs demonstrate high therapeutic efficacy through the synergistic effect of combined chemo-photothermal treatment. *In vivo* studies demonstrate marked suppression of tumor growth in mice bearing rat C6 glioblastoma after the administration with single intratumoral injection of PTX-loaded FMP-CNS.

Introduction

Multifunctional drug delivery nanoparticles with high payload, controlled drug release, and imaging capability are highly desirable in medicine to increase therapeutic efficacy, minimize adverse effects of cytoxic drugs, and facilitate treatment monitoring.[1-8] As many chemotherapeutic drugs are poorly water-soluble, much effort has been focused on the development of multifunctional drug delivery nanomaterials for delivering hydrophobic drugs.[9-12] To date, a number of nanocarriers, including carbon nanotubes, magnetic nanoparticles, peptides, liposomes, mesoporous silica nanoparticles, lipid and polymeric nanoparticles have been investigated to deliver hydrophobic drugs, reduce side effects, and

---

mzhang@u.washington.edu (M Zhang), shuiqin.zhou@csi.cuny.edu (S. Zhou).

Electronic Supplementary Information (ESI) available: Experimental details, Fig. S1-S14 and Tables S1-S2. See DOI: 10.1039/x0xx00000x improve therapeutic outcomes.[13-17] While the side effects of hydrophobic drugs have indeed been reduced, the current nanocarrier formulations still suffer from some limitations. For example, covalent conjugation of hydrophobic drugs onto nanocarriers has very low drug loading capacity (PTX, ~10 wt%), leading to inadequate therapeutic efficacy.[17] Hydrophobic drug molecules loaded in liposomes or nanoparticles such as micelle and lipid nanaoparticles by hydrophobic interactions often exhibit burst release rather than sustained release. Further, most nanocarriers do not provide controlled release of pre-loaded drug molecules in response to a given stimulus.[18, 19]

Mesoporous silica nanoparticles (MSNs) with ajustable pore sizes and large surface areas are an alternative delivery system that improves the drug loading capacity and release behavior.[20-25] Typically, the loading capacity of MSNs for the hydrophobic drug can not be higher than 30 wt%.[26] Most MSNs exhibit weak hydrophilicity for water dispersion and/or potentail toxicity for in vivo applications; drug-loaded MSNs could easily flocculate when used in aqueous solutions.[25, 27, 28] Also MSNs generally lack intrinsic optical properties for imaging and do not have controlled-drug release capacity.[29-30] In contrast to MSN-based nanocarriers, mesoporous carbon nanoparticles (MCN) demonstrate lower cytotoxicity and higher drug loading capacity due to their combined higher surface areas and pore volumes and to their carbon hydrophobic interaction with hydropbic drugs.[32-36] However, existing MCNs lack wavelength-tunable fluorescent properties for NIR optical imaging and/or photothermal effect for light-responsive drug release.[37-42] Recently, fluorescent carbon quantum dots have attracted attention because of their unique optical properties, good aqueous stability and excellent photothermal effect.[43-45] The small size and surface area of these quantum dots, however, limit their loading capacity for hydrophobic drugs.[46, 47]

In this study, we developed a simple fluorescent, mesoporous carbon nanoshell (FMP-CNS) as a hydrophobic drug carrier that bears functions of stimuli-responsive drug release, multimodal optical imaging, and combined photothermal/chemo-therapy. The synthesis of FMP-CNSs is a simple and high yield process. FMP-CNSs exhibits sustainable and wavelength-tunable fluorescence properties and functions as a multi-modal optical imaging agent under a broad range of excitation wavelength from 405 nm to 900 nm. PTX, a hydrophobic drug, is chosen as a model drug to demonstrate our nanocarrier due to its excellent stability and being primary chemotherapy drug for glioblastoma (GBM), cell lung cancers, breast cancers, and ovarian carcinoma.[48, 49] Our results showed that FMP-CNSs demonstrate a high-level PTX loading capacity. Furthermore, FMP-CNSs can effectively absorb the near infrared (NIR) light and convert it to heat, thus, establishing an NIR-responsive drug release capability and combined photothermal/chemo-therapeutic efficacy as demonstrated both *in vitro* and *in vivo*.

Results and discussion

Synthesis and characterization of FMP-CNSs

Fig. 1a is the schematic represenation of the formation FMP-CNSs. FMP-CNSs are obtained by a three-step process. In step I, uniform and monodispersed SiO_2@FMP-CNSs nanoparticles (Fig. S1) are prepared by a solvothermal method using SiO_2 nanoparticles as a template and 3-aminophenylboronic acid (APBA) as a carbon precursor. APBA molecules are adsorbed onto the surface of charged SiO_2 through the electrostatic attraction between the positively charged amino groups of APBA molecules and the negatively charged SiO_2 and the hydrogen bonding between the hydroxyl groups on APBA molecules and SiO_2 surface. Under high temperature (200°C) and pressure produced by the gasification of solvent acetone in a sealed reactor, the chemical bond of C-H in the APBA molecules is ruptured, leading to the formation of carbon-based free radicals. These small carbon-based free radicals further form relatively large carbon-based fragments with disordered (amorphous carbon) or ordered (graphene quantum dots) structure due to the chemical bond between conjugated double bonds of carbon-based free radicals. These carbon-based fragments on SiO_2 are highly mobile and form a loosened coating layer containing amorphous carbon and graphene quantum dots on SiO_2. Meanwhile, the O_2 decomposed from the H_2O_2 rapidly reacts with the carbon fragments to generate the hydrophilic hydroxyl and carboxyl groups on the surface of carbon-based fragments. In step II, complete erosion of the SiO_2 core is achieved by mixing SiO_2@FMP-CNSs nanoparticles with ammonia water at 200°C to form FMP-CNSs.

The morphology and structure of the as-prepared FMP-CNSs were characterized by transmission electron microscopy (TEM). TEM image in Fig. 1b shows that FMP-CNSs have a good monodispersity and hollow cavity. SEM image (Fig. S2) of FMP-CNSs indicates their highly uniform spherical nanostructure with a average diameter of ~70 nm. The high-magnification TEM image (inset in Fig. 1b) of a single FMP-CNS further indicate that the carbon shell has a thickness of 15 nm. The crystallinity and phase of FMP-CNSs were investigated by Raman spectroscopy (Fig. 1c). The peak at 1581 cm^{-1} (G-band) is associated with the E_{2g} mode of graphite, which is related to the vibration of sp^2-hybridized carbon atoms in a two-dimensional hexagonal lattice.[50, 51] The peak at 1340 cm^{-1} (D band) is ascribed to the vibration of carbon atoms with dangling bonds in the termination plane of disordered graphite or glassy carbon.[52] The low intensity ratio of D-band to G-band (I_D/I_G) suggests that FMP-CNSs exhibit an appreciable degree of graphitization. The crystallographic structure of the as-prepared FMP-CNSs was further examined by X-ray powder diffraction (XRD). The observed characteristic reflection of 002 in the XRD pattern (Fig. S3a) can be indexed to the bulk graphite.[53] The XPS survey spectrum (Fig. S3b) reveals that carbon (78.8%), oxygen (15.3%), nitrogen (4.5%) and boron (1.4%) are present on the surface of FMP-CNSs.

The surface property of FMP-CNSs was characterized by FT-IR, as shown in Fig. S4. An absorption peak of the -OH group at 3380 cm^{-1} and a C=O stretching mode at 1704 cm^{-1}, respectively, of the carboxylic acid groups conjugated with condensed aromatic carbons were observed.[54] These peaks indicate the presence of the carboxyl and hydroxyl groups on FMP-CNSs. The hydrodynamic diameter (D_h) (Fig. 1d) of FMP-CNSs is about 82.5 nm in water with narrow size distribution, suggesting that they are very stable in water and do not form aggregates. In addition, FMP-CNSs were well-dispersed in cell culture medium containing 10 % serum and indicated excellent stability in 7 days (Fig. S5).

The UV–Vis absorption spectrum (Fig. 1e) of FMP-CNSs shows a sharp absorption at ~242 nm, which is ascribed to the π-π^* transition of aromatic domains in the carbon shell.[55] A shoulder peak at 288 nm is also observed, which is possibly attributable to n-π^* transition of

C=O bonds in the carbon shell.[56] Furthermore, a weak absorption in the NIR region of 650–900 nm of FMP-CNSs at low concentration (1 μg/mL) was observed (Fig. S6), which may result from the aromatic, highly π-conjugated carbon structure and suggest that the nanocarrier can serve as a photothermal agent.[57] When the aqueous dispersion of FMP-CNSs was exposed to a UV lamp with a light wavelength of 365 nm, a green light was emitted and readily observed (inset in Fig. 1e).

The photoluminescence (PL) property of FMP-CNSs was studied and preformed under different excitation wavelengths (λ_{ex}). As shown in Fig. 1f, when λ_{ex} increases from 240 nm to 540 nm, the emission peak gradually shifts to longer wavelengths and the PL intensity gradually increases and then decreases. This tunable PL property (emission wavelength and intensity) of FMP-CNSs can be attributed to the quantum confinement of conjugated π-electrons in an sp^2 network and the nitrogen and boron atom doping, which induces significant local distortion and thus creates various energy gaps.[58-60] The PL quantum yield of FMP-CNSs was determined to be 9.5% using rhodamine B as a standard (Table S1). FMP-CNSs also demonstrate excellent photostability since only slight change (Fig. S7) in PL intensity was observed after 2 h continuous exposure of FMP-CNS solution to the excitation light of λ_{ex} = 360 nm in a fluorospectrometer. More importantly, the PL spectra (Fig. 1g) of FMP-CNSs excited by long-wavelength light from 980 to 740 nm clearly demonstrate upconverted emissions from 535 to 454 nm. The upconversion PL behavior of FMP-CNSs can be attributed to their multiphoton active processes.[61] These results indicate that FMP-CNSs can be used as excellent optical marker for bioimaging without need of organic dyes which are mostly short-lived and costly.

Multi-modal optical imaging of FMP-CNSs

After confirming the strong fluorescence capability and tunable emission wavelength of FMP-CNSs, SF-763 human GBM cells were selected as a model to evaluate the optical cellular imaging function of these FMP-CNSs as a fluorescent marker. Fig. 2 a-c shows the laser scanning confocal images of SF-763 cells incubated with FMP-CNSs under laser irradiation at wavelengths of 405, 488, and 546 nm, respectively. Results show that FMP-CNSs produced a bright fluorescence and can illuminate SF-763 cells in multicolor forms. Meanwhile, the confocal images (Fig. S8) of SF-763 cells did not show a fluorescent signal change after 14 days, which indicates that FMP-CNSs have excellent photostability and can be used for long-term cellular imaging. Fig. 2 d-f show images of two-photon fluorescence (d), DAPI nuclear stained (e) and their overlay (f) of SF-763 cells after uptaking FMP-CNSs and excited by a wavelength of 900 nm. It is clear that the cells can be also illuminated by the upconverted fluorescence emitted by FMP-CNSs under excitation of an NIR laser.

In vivo NIR imaging is now widely utilized owing to their high photon tissue penetration with reduced background autofluorescence.[62] To investigate possible application of FMP-CNSs for *in vivo* NIR imaging, they (100 μL, 1mg/mL) were injected into nude mouse subcutaneously at two different spots on the back. The mouse was then imaged using an IVIS *in vivo* imaging system. As shown in Fig. 2g-l, fluorescence of FMP-CNSs can be observed at excitation wavelengths of 605, 640, 675, 710 and 745 nm. Furthermore, the PL spectra of FMP-CNSs confirmed their NIR emission under different excitation wavelengths.

The capability of FMP-CNSs for NIR *in vivo* fluorescence imaging indicates their potential uses as optical nanoprobes in biomedical imaging.

Drug loading and release of FMP-CNSs

Full nitrogen sorption isotherms were measured to quantify specific surface area and pore sizes of FMP-CNSs. As shown in Fig. 3a, N_2 sorption–desorption isotherms exhibit II-type curves for FMP-CNSs, which is typical for mesoporous materials. The determined Brunauer–Emmett–Teller (BET) surface area and total pore volume of FMP-CNSs are 259.99 $m^2 g^{-1}$ and 0.38 $cm^3 g^{-1}$, respectively. The surface area of FMP-CNSs is larger than the reported hollow carbon nanospheres (239.5 $m^2 g^{-1}$) and hollow carbon dots (16.4 $m^2 g^{-1}$).[8,46] However, FMP-CNSs has a surface area smaller than the reported hydrophilic mesoporous carbon nanoparticles (864 $m^2 g^{-1}$).[37] The average Barrett–Joyner–Halenda (BJH) pore diameters (Fig. S10) of FMP-CNSs calculated from the desorption branch of the isotherm range from 1.9 nm to 4.8 nm. The hollow inner structure, mesoporous carbon shell and large surface area of FMP-CNSs are suitable as carriers for drug delivery application. The drug loading capacity of FMP-CNSs was tested by mixing of PTX in ethanol solution with aqueous solution of FMP-CNSs and quantified by HPLC-MS of initial PTX solution and separated PTX solution (Fig. 3b). The drug loading capacity of FMP-CNSs for PTX was 800.4 mg/g (~80.4 wt%), which is much higher than that previously-reported other mesoporous silica-based nanocarriers and hybrid micelles (<30.9 wt%).[26,63, 64] The appearance of the characteristic UV-Vis absorption peak of PTX at around 200 nm (Fig. 3d) confirms the successful loading of PTX molecules in FMP-CNSs.

The high drug loading capacity of FMP-CNSs can be attributed to several factors. First, the large surface areas of central hollow cavity and mesoporous carbon shell provide ample space for drug storage. Second, PTX molecules interact with FMP-CNSs through the supramolecular π-stacking between the conjugated rings of PTX molecules and aromatic rings of FMP-CNSs as well as the hydrogen bonding between the hydroxyl group of PTX and surface carboxyl group of FMP-CNSs. Third, the use of two solvents (ethanol and water) rather than ethanol alone in drug loading also promotes the drug loading. For example, after PTX dispersed in ethanol enters FMP-CNSs in DI water by diffusion (Fig. S11a), the ethanol would escapes from FMP-CNSs, and PTX tend to remains in FMP-CNSs due to the strong molecule interactions between PTX and FMP-CNSs as well as the repulsion from hydrophilic water molecules outside of FMP-CNS shell. When the process of loading PTX was carried out in ethanol only (i.e., PTX in ethanol with FMP-CNSs in ethanol) (Fig. S11b), the drug loading capacity of FMP-CNSs for PTX is only 20%. In this case, PTX molecules were loaded into FMP-CNSs due to the molecule interactions between PTX and FMP-CNSs but in the absence of water repulsion. The appearance of the characteristic UV-Vis absorption peak of PTX at around 200 nm (Fig. 3c) confirms the successful loading of PTX molecules in FMP-CNSs with ethanol only. However, the high absorption intensities at 200 nm and 230 nm indicate that the drug loading of FMP-CNSs for hydrophobic anti-cancer PTX is more efficient in the mixing solvent than in ethanol only. Furthermore, the red-shift of the characteristic UV absorption peak for PTX at 229 nm after PTX was loaded in FMP-CNSs confirms the supramolecular π-stacking between the conjugated rings of PTX molecules and aromatic rings of FMP-CNSs.

The *in vitro* release of PTX from PTX-loaded FMP-CNSs was investigated using a dialysis membrane against a saline solution. Fig. 3d compares the PTX release behaviors from the PTX-loaded FMP-CNSs dispersed in PBS solution at 37 °C, with and without NIR light irradiation. Without NIR radiation, the release of PTX from FMP-CNSs is slow at a nearly steady rate after 10 h. In contrast, a short 5-min exposure to NIR light can speed up the release of PTX from FMP-CNSs. When the radiation was turned off, the heating ceases and the drug release returns to its regular slow rate. The significantly increased drug release rate under NIR light exposure can be attributed to the local heating of FMP-CNSs produced by the efficient photothermal conversion of the fluorescent carbon shell. Fig. 3e confirms the photothermal effect of FMP-CNSs upon exposure to NIR light (825 nm) at a power density of 1.5 W/cm^2, which results in a temperature increase of near 26 °C within 5 min. In comparison, the temperature change of water (control) was much less significant under the same irradiation condition. The IR thermal imaging (Fig. 3f) of FMP-CNSs further verifies their photothermal conversion effect after irradiation by NIR light for 5 min. Such photothermal effect of FMP-CNSs not only weakens the drug-host interaction but also increases the mobility of PTX at elevated temperatures, therefore, increase the release rate of PTX from FMP-CNSs.

Biocompatibility and biodistribution of FMP-CNSs

To evaluatethe therapeutic efficacy of FMP-CNSs in vitro, we firstly tested their cytotoxicity in SF-763 cells. FMP-CNSs had negligible cytotoxicity against SF-763 cells after 72 h incubation at 4 μg/mL (Fig. 4a). In contrast, cell viability dramatically decreased when incubated with PTX-loaded FMP-CNSs. To investigate the photothermal effect of nanoparticles, SF-763 cells were irradiated with NIR light (1.5 W/cm^2) for 5 min during the incubation with FMP-CNSs or PTX-loaded FMP-CNSs. Increased cell killing of FMP-CNSs can be observed with the addition of 5 min NIR irradiation even though the concentration of FMP-CNSs was only 4 μg/mL. In contrast, NIR irradiation alone has negligible effect on cell viability (Fig. S12). Importantly, combinatory treatment with PTX loaded FMP-CNSs along with NIR irradiation had more pronounced effect than the individual treatments. The cytotoxicity of FMP-CNSs with different treatments was summarized in Table S2. Therapeutic efficacies of FMP-CNSs as PTX carriers and photothermal therapy agents (calculated by subtracting the cell viability from 100%) for cells treated by (1) chemotherapy alone, (2) photothermal treatment alone, (3) additive chemotherapy and photothermal therapy, and (4) combined chemo-photothermal therapy is shown in Fig. 4b. The additive efficacy was estimated using the relation $T_{additive} = 100 - (f_{chemo} \times f_{photothermal}) \times 100$, where f_{chemo} and $f_{photothermal}$ are the fraction of surviving cells after independent chemotherapy and photothermal therapy, respectively.[65] The combined chemo-photothermal therapy induced significantly higher cytotoxicity than the additive therapeutic, indicating the synergistic effect of PTX-loaded FMP-CNSs treatment.

To examine the biodistribution and possible toxic effects of FMPCNSs, healthy mice were injected with 200 μL of 1 mg/mL of FMPCNSs via tail vein and mice receiving no injection were used as controls. Mice were euthanized and whole organs of liver, spleen, kidney, lung, and heart were harvested at different time points post injection. FMP-CNSs in major organs were assessed by measuring the fluorescence intensity of FMP-CNSs using an IVIS imaging system. As shown in Fig. 4c, liver was the dominant organ in accumulation of FMP-CNSs at 24 h post-injection because of reticuloendothelial system (RES) uptake, followed by the kidney, spleen, lung, and heart. At 96 h post-injection, less than 20% of initially-accumulated FMP-CNSs remained in liver and minimal amounts of FMP-CNSs were found in heart, kidney, lung, and spleen (Fig. 4d). Histological analysis on major organs was performed to evaluate the tissue compatibility of FMP-CNSs *in vivo*. Tissues were harvested from mice at 96 h after FMP-CNSs injection, fixed in 10% formalin, embedded in paraffin, sectioned, and stained with hematoxylin and eosin (H&E). As shown in Fig. 4e, no discernible differences in cell morphology and tissue structure were observed between treated mice and control mice, suggesting that FMP-CNSs have good tissue compatibility.

In vivo therapy of FMP-CNSs

To examine the efficacy of FMP-CNSs on treating tumors in vivo, mice bearing C6 GBM tumors were administrated with FMP-CNSs (200 μL, 1mg/mL) by a single intratumoral injection and tumors were then subjected or not subjected (irradiation control) to NIR irradiation (825 nm, 1.5 W/cm^2) for 5 min at 24 h post injections. Tumor-bearing mice were randomly divided into 4 groups with five mice per group, and each group were treated with PBS + NIR irradiation (control), PTX-loaded FMP-CNSs without NIR irradiation (i.e., chemotherapy only), FMP-CNSs (photothermal therapy only), or PTX-loaded FMP-CNSs (combined therapy) + NIR (825 nm) irradiation for 5 min at 1.5 W/cm^2. Tumor sizes in mice were measured every two days up to 12 days post-treatment. As shown in Fig. 5a and b, the tumors in control mice grew rapidly, and NIR irradiation alone did not show observable effect on tumor growth (Fig. S13). The tumors in mice treated with PTX-loaded FMP-CNSs showed a significant reduction in tumor growth as compared to those in control mice. A reduction in tumor growth was also observed in mice treated with FMP-CNSs (no PTX, particle control) + NIR irradiation. When NIR irradiation was applied to mice treated with PTX-loaded FMP-CNSs, a suppression in tumor growth by this combined photothermal/chemo treatment was much higher than that of additive photothemal- and chemotherapy alone, demonstrating a synergistic therapeutic effect. Without active targeting function, the accumulation of PTX-loaded FMP-CNSs in tumors likely resulted from two mechanisms: the enhanced permeability and retention (EPR) of NPs and the NP-induced endothelial leakiness known as “NanoEL” which causes a leaky phenotype to enhance the access to tumors.[66-69] Notably, the NIR fluorescence signal (Fig. S14) of FMP-CNSs is also observed in tumor at an excitation wavelength of 745 nm, which indicates their potential to serve in NIR imaging-guided therapy.

At day 12, tumors from all mice were harvested and weighed. As shown in Fig. 5c, compared to photothermal therapy or chemo-therapy alone, the combined treatment (PTX-loaded FMP-CNSs + NIR irradiation) resulted in the smallest tumor, which collolate the tumor growth curve. This high therapeutic efficacy of combined chemo- and photothermaltherapy using PTX-loaded FMP-CNSs with a single injection might be attributed to much higher drug loading capacity exhibited by our nanocarriers than existing nanocarriers (80 wt% vs 20 wt%), the increased drug release under NIR irradiation, and the increased cell membrane permeability and internalization caused by local heating of FMP-CNSs. The last phenomena was also observed in other studies intended to improve the treatment efficiency through combined photothermal/chemo therapy.[70, 71] H&E staining of tumor sections (Fig. 5d) further confirmed that cells in tumors from the control group largely retained their normal morphology with distinctive membranes and nuclear structures while most tumor cells from the treated mice, especially those receiving the combined treatment, were severely damaged with loss of nuclei. No obvious body weight drop of the mice was observed for all treatment groups.

Conclusions

We have synthesized a multifunctional mesoporous carbon nanoshell via a simple method using SiO_2 nanosphere as a template and APBA as a carbon precursor. The as-synthesized FMP-CNSs exhibit excitation wavelength-tunable photoluminescence, which allows FMP-CNSs to serve as a sustainable confocal, two-photon fluorescence, and NIR imaging contrast agent. The central hollow cavity, mesoporous structure of the carbon shell, and the surface carboxyl/hydroxyl groups endow FMP-CNSs with high drug loading capacity for hydrophobic anti-cancer drugs and excellent dispersibility in aqueous solutions, respectively. FMP-CNSs exhibit NIR-responsive drug release property and combined photothermo/chemotherapy efficacy. Notably, the combined treatment with chemo- and photothermaltherapy marked high therapeutic efficacy via a single intratumoral injection in vivo. This carbon nanoshell demonstrates great promise for simultaneous imaging diagnostics and treatment.

Supplementary Material

Refer to Web version on PubMed Central for supplementary material.

Acknowledgements

We gratefully acknowledge the financial support from NIH grant (R01CA161953), Kyocera professor endowment, and American Diabetes Association (Basic Science Award 1-12-BS-243). The two photon fluorescence imaging study was supported in part by a gift to the Institute for Stem Cell and Regenerative Medicine at the University of Washington.

References

1. Mura S, Nicolas J, Couvreur P. Nat Mater. 2013; 12:991–1003. [PubMed: 24150417]
2. Horcajada P, Chalati T, Serre C, Gillet B, Sebrie C, Baati T, Eubank JF, Heurtaux D, Clayette P, Kreuz C, Chang J-S, Hwang YK, Marsaud V, Bories P-N, Cynober L, Gil S, Ferey G, Couvreur P, Gref R. Nat Mater. 2010; 9:172–178. [PubMed: 20010827]
3. Song J, Yang X, Jacobson O, Lin L, Huang P, Niu G, Ma Q, Chen X. ACS Nano. 2015; 9:9199–9209. [PubMed: 26308265]
4. Chen Q, Liang C, Wang C, Liu Z. Adv. Mater. 2015; 27:903–910. [PubMed: 25504416]
5. Zhao P, Zheng M, Luo Z, Gong P, Gao G, Sheng Z, Zheng C, Ma Y, Cai L. Sci. Rep. 2015; 5:14258. [PubMed: 26400780]
6. Wang H, Di J, Sun Y, Fu J, Wei Z, Matsui H, del C. Alonso A, Zhou S. Adv. Funct. Mater. 2015; 25:5537–5547.
7. Liu G, Zhou L, Su Y, Dong C-M. Chem. Commun. 2014; 50:12538–12541.
8. Wang H, Sun Y, Yi J, Fu J, Di J, del Carmen Alonso A, Zhou S. Biomaterials. 2015; 53:117–126. [PubMed: 25890712]
9. Lipinski CA. J. Pharmacol. Toxicol. Methods. 2000; 44:235–249. [PubMed: 11274893]

10. Merisko-Liversidge EM, Liversidge GG. Toxicol. Pathol. 2008; 36:43–48. [PubMed: 18337220]
11. Liu Z, Robinson JT, Sun X, Dai H. J. Am. Chem. Soc. 2008; 130:10876–10877. [PubMed: 18661992]
12. Farokhzad OC, Langer R. ACS Nano. 2009; 3:16–20. [PubMed: 19206243]
13. Liu Z, Chen K, Davis C, Sherlock S, Cao Q, Chen X, Dai H. Cancer Res. 2008; 68:6652–6660. [PubMed: 18701489]
14. Zhang P, Cheetham AG, Lin YA, Cui H. ACS Nano. 2013; 7:5965–5977. [PubMed: 23758167]
15. Meng H, Wang M, Liu H, Liu X, Situ A, Wu B, Ji Z, Chang CH, Nel AE. ACS Nano. 2015; 9:3540–3557. [PubMed: 25776964]
16. Han, L.-m., Guo, J., Zhang, L.-j., Wang, Q.-s., Fang, X.-l. Acta Pharmacol. Sin. 2006; 27:747–753. [PubMed: 16723095]
17. Liu D, Wu W, Chen X, Wen S, Zhang X, Ding Q, Teng G, Gu N. Nanoscale. 2012; 4:2306–2310. [PubMed: 22362270]
18. Mu Q, Jeon M, Hsiao MH, Patton VK, Wang K, Press OW, Zhang M. Adv Healthc Mater. 2015; 4:1236–1245. [PubMed: 25761648]
19. Caldorera-Moore ME, Liechty WB, Peppas NA. Acc. Chem. Res. 2011; 44:1061–1070. [PubMed: 21932809]
20. Wang Y, Yan Y, Cui J, Hosta-Rigau L, Heath JK, Nice EC, Caruso F. Adv. Mater. 2010; 22:4293–4297. [PubMed: 20564713]
21. Li Z, Barnes JC, Bosoy A, Stoddart JF, Zink JI. Chem. Soc. Rev. 2012; 41:2590–2605. [PubMed: 22216418]
22. Tarn D, Ashley CE, Xue M, Carnes EC, Zink JI, Brinker CJ. Acc. Chem. Res. 2013; 46:792–801. [PubMed: 23387478]
23. Lu J, Liong M, Zink JI, Tamanoi F. Small. 2007; 3:1341–1346. [PubMed: 17566138]
24. Slowing II, Vivero-Escoto JL, Wu C-W, Lin VSY. Adv. Drug Del. Rev. 2008; 60:1278–1288.
25. Hudson SP, Padera RF, Langer R, Kohane DS. Biomaterials. 2008; 29:4045–4055. [PubMed: 18675454]
26. Wang H, Wang K, Tian B, Revia R, Mu Q, Jeon M, Chang F-C, Zhang M. Small. 2016; 12:6388–6397. [PubMed: 27671114]
27. Fadeel B, Garcia-Bennett AE. Adv. Drug Del. Rev. 2010; 62:362–374.
28. Liong M, Lu J, Kovochich M, Xia T, Ruehm SG, Nel AE, Tamanoi F, Zink JI. ACS Nano. 2008; 2:889–896. [PubMed: 19206485]
29. Li X, Zhou L, Wei Y, El-Toni AM, Zhang F, Zhao D. J. Am. Chem. Soc. 2014; 136:15086–15092. [PubMed: 25251874]
30. Li N, Yu Z, Pan W, Han Y, Zhang T, Tang B. Adv. Funct. Mater. 2013; 23:2255–2262.
31. Lai C-Y, Trewyn BG, Jeftinija DM, Jeftinija K, Xu S, Jeftinija S, Lin VSY. J. Am. Chem. Soc. 2003; 125:4451–4459. [PubMed: 12683815]
32. Hu B, Wang K, Wu L, Yu SH, Antonietti M, Titirici MM. Adv. Mater. 2010; 22:813–828. [PubMed: 20217791]
33. Kim TW, Chung PW, Slowing II, Tsunoda M, Yeung ES, Lin VS. Nano Lett. 2008; 8:3724–3727. [PubMed: 18954128]
34. Ryoo R, Joo SH, Jun S. The Journal of Physical Chemistry B. 1999; 103:7743–7746.
35. Ma P, Xiao H, Li X, Li C, Dai Y, Cheng Z, Jing X, Lin J. Adv. Mater. 2013; 25:4898–4905. [PubMed: 23857588]
36. Chen Y, Chen HR, Shi JL. Acc. Chem. Res. 2014; 47:125–137. [PubMed: 23944328]
37. Gu J, Su S, Li Y, He Q, Shi J. Chem. Commun. (Camb.). 2011; 47:2101–2103. [PubMed: 21183990]
38. Chen Y, Xu P, Wu M, Meng Q, Chen H, Shu Z, Wang J, Zhang L, Li Y, Shi J. Adv. Mater. 2014; 26:4294–4301. [PubMed: 24687452]
39. Qiao ZA, Guo B, Binder AJ, Chen J, Veith GM, Dai S. Nano Lett. 2013; 13:207–212. [PubMed: 23256449]
40. Zhu J, Liao L, Bian X, Kong J, Yang P, Liu B. Small. 2012; 8:2715–2720. [PubMed: 22674566]

41. Zhou L, Dong K, Chen Z, Ren J, Qu X. Carbon. 2015; 82:479–488.
42. Wang H, Zhou S. Biomaterials Science. 2016; 4:1062–1073. [PubMed: 27184106]
43. Cao L, Wang X, Meziani MJ, Lu F, Wang H, Luo PG, Lin Y, Harruff BA, Veca LM, Murray D, Xie S-Y, Sun Y-P. J. Am. Chem. Soc. 2007; 129:11318–11319. [PubMed: 17722926]
44. Zhu S, Meng Q, Wang L, Zhang J, Song Y, Jin H, Zhang K, Sun H, Wang H, Yang B. Angew. Chem. Int. Ed. 2013; 52:3953–3957.
45. Ge J, Jia Q, Liu W, Guo L, Liu Q, Lan M, Zhang H, Meng X, Wang P. Adv. Mater. 2015; 27:4169–4177. [PubMed: 26045099]
46. Wang Q, Huang X, Long Y, Wang X, Zhang H, Zhu R, Liang L, Teng P, Zheng H. Carbon. 2013; 59:192–199.
47. Alexis F, Pridgen E, Molnar LK, Farokhzad OC. Mol. Pharm. 2008; 5:505–515. [PubMed: 18672949]
48. Ng VG, Mena C, Pietras C, Lansky AJ. Eur. J. Clin. Invest. 2015; 45:333–345. [PubMed: 25615282]
49. Luo B, Xu S, Luo A, Wang W-R, Wang S-L, Guo J, Lin Y, Zhao D-Y, Wang C-C. ACS Nano. 2011; 5:1428–1435. [PubMed: 21284377]
50. Tian L, Ghosh D, Chen W, Pradhan S, Chang X, Chen S. Chem. Mater. 2009; 21:2803–2809.
51. Ferrari AC, Robertson J. Physical Review B. 2000; 61:14095–14107.
52. Ristein J, Stief RT, Ley L, Beyer W. J. Appl. Phys. 1998; 84:3836–3847.
53. Wu X, Tian F, Wang W, Chen J, Wu M, Zhao JX. Journal of Materials Chemistry C. 2013; 1:4676–4684.
54. Duffy P, Magno LM, Yadav RB, Roberts SK, Ward AD, Botchway SW, Colavita PE, Quinn SJ. J. Mater. Chem. 2012; 22:432–439.
55. Chang Y-R, Lee H-Y, Chen K, Chang C-C, Tsai D-S, Fu C-C, Lim T-S, Tzeng Y-K, Fang C-Y, Han C-C, Chang H-C, Fann W. Nat Nano. 2008; 3:284–288.
56. Eda G, Lin Y-Y, Mattevi C, Yamaguchi H, Chen H-A, Chen IS, Chen C-W, Chhowalla M. Adv. Mater. 2010; 22:505–509. [PubMed: 20217743]
57. Robinson JT, Tabakman SM, Liang Y, Wang H, Sanchez Casalongue H, Vinh D, Dai H. J. Am. Chem. Soc. 2011; 133:6825–6831. [PubMed: 21476500]
58. Li L, Wu G, Yang G, Peng J, Zhao J, Zhu J-J. Nanoscale. 2013; 5:4015–4039. [PubMed: 23579482]
59. Cao L, Meziani MJ, Sahu S, Sun Y-P. Acc. Chem. Res. 2013; 46:171–180. [PubMed: 23092181]
60. Wang H, Zhuang J, Velado D, Wei Z, Matsui H, Zhou S. ACS Applied Materials & Interfaces. 2015; 7:27703–27712. [PubMed: 26615668]
61. Lee E, Ryu J, Jang J. Chem. Commun. 2013; 49:9995–9997.
62. Frangioni JV. Curr. Opin. Chem. Biol. 2003; 7:626–634. [PubMed: 14580568]
63. Kutty RV, Tay CY, Lim CS, Feng S-S, Leong DT. Nano Research. 2015; 8:2533–2547.
64. Kutty RV, Chia SL, Setyawati MI, Muthu MS, Feng S-S, Leong DT. Biomaterials. 2015; 63:58–69. [PubMed: 26081868]
65. Hahn GM, Braun J, Har-Kedar I. Proc. Natl. Acad. Sci. U. S. A. 1975; 72:937–940. [PubMed: 48253]
66. Setyawati MI, Tay CY, Leong DT. Nanomedicine. 2014; 9:369–371.
67. Tay CY, Setyawati MI, Xie J, Parak WJ, Leong DT. Adv. Funct. Mater. 2014; 24:5936–5955.
68. Setyawati MI, Tay CY, Docter D, Stauber RH, Leong DT. Chem. Soc. Rev. 2015; 44:8174–8199. [PubMed: 26239875]
69. Setyawati MI, Tay CY, Chia SL, Goh SL, Fang W, Neo MJ, Chong HC, Tan SM, Loo SCJ, Ng KW, Xie JP, Ong CN, Tan NS, Leong DT. Nature Communications. 2013; 4:1673.
70. Wang C, Xu H, Liang C, Liu Y, Li Z, Yang G, Cheng L, Li Y, Liu Z. ACS Nano. 2013; 7:6782–6795. [PubMed: 23822176]
71. Feng L, Yang X, Shi X, Tan X, Peng R, Wang J, Liu Z. Small. 2013; 9:1989–1997. [PubMed: 23292791]

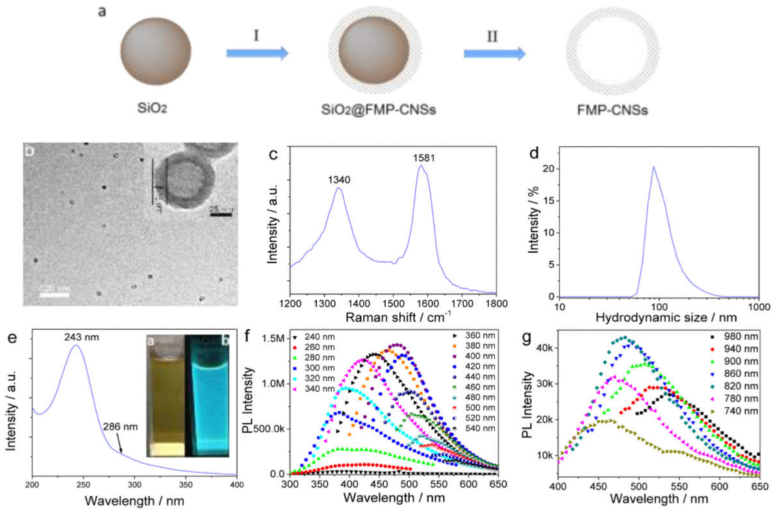

Fig. 1.

Synthesis and characterization of FMP-CNSs. (a) a schematic of formation of FMP-CNSs. I: surface coating of SiO_2; II: erosion of the SiO_2 and formation of FMP-CNCs. (b) TEM image, (c) Raman spectrum and (d) hydrophilic size distribution of FMP-CNSs. (e) UV-Vis absorption spectrum of FMP-CNSs, the inset is photograph of aqueous dispersions of FMP-CNSs under (left, a) visible light and (right, b) UV light (365 nm); (f) and (g) PL spectra and upconverted PL spectra of FMP-CNSs obtained with different excitation wavelengths.

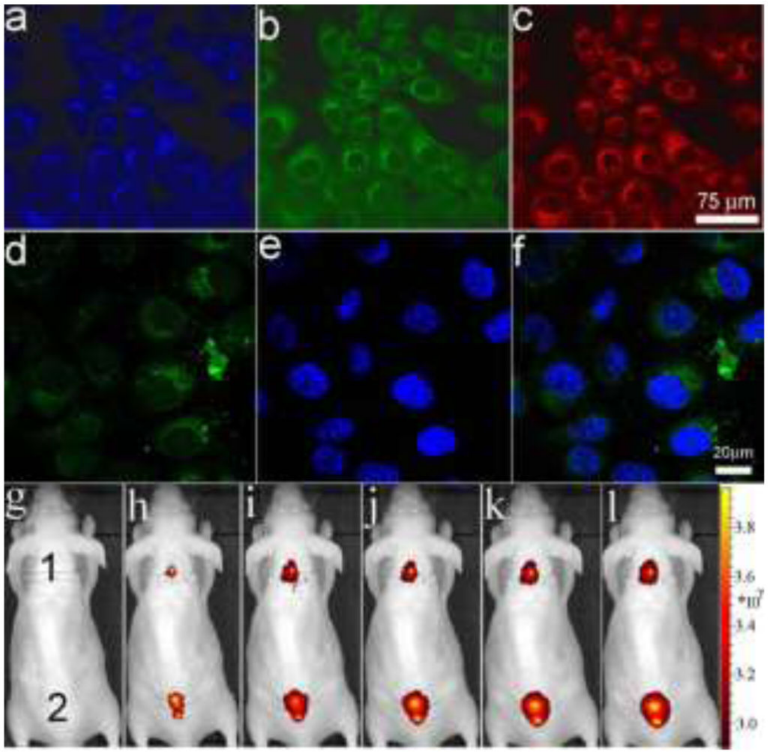

Fig. 2.

Laser scanning confocal fluorescence images of SF-763 cells incubated with FMP-CNSs under different excitation wavelengths: (a) 405 nm; (b) 488 nm; (c) 546 nm. (d) two-photon fluorescence with a excitation wavelength of 900 nm, (e) DAPI nuclear stain, and (f) overlaid images of SF-763 cells incubated with FMP-CNSs. *In vivo* NIR fluorescence images of FMP-CNSs-injected mouse under various excitation wavelengths: (g) white light, (h) 605, (i) 640, (j) 675, (k) 710, and (l) 745 nm.

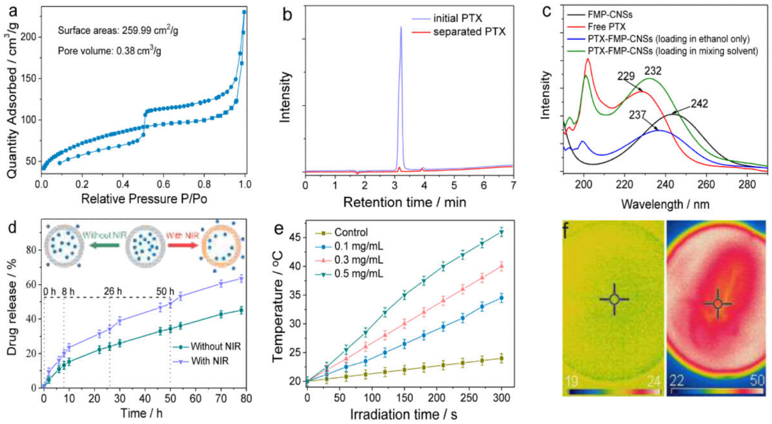

Fig. 3.

Mesoporous properties and drug loading and release of FMP-CNSs. (a) N_2 adsorption/desorption isotherms of FMP-CNSs. (b) HPLC analysis of initial PTX solution and separated PTX solution. (c) UV absorption spectra of free PTX in ethanol, FMP-CNSs in ethanol, PTX-FMP-CNSs (loading in mixing solvent) in ethanol, and PTX-FMP-CNSs (loading in ethanol only) in ethanol. (d) Release behavior of PTX from PTX-loaded FMP-CNSs. Inset: the release schematic of PTX from FMP-CNSs with/without NIR irradiation. (e) Photothermal heating curves of pure water (control) and FMP-CNSs (0.1, 0.3 and 0.5 mg/mL) in water under 825 nm laser irradiation at a power of 1.5 W/cm^2 for 5 min. (f) IR thermal images of FMP-CNSs (0.5 mg/mL) in water under irradiation for 0 min (left) and 5 min (right).

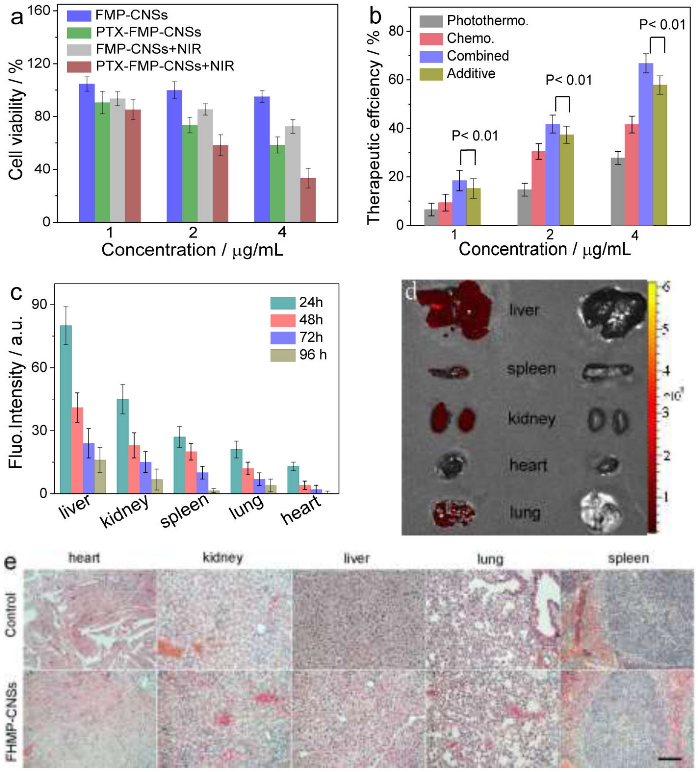

Fig. 4.

In vitro and *in vivo* biocompatibility assessment. (a) *In vitro* cytotoxicity of FMP-CNSs and PTX-loaded FMP-CNSs with or without NIR irradiation at 1.5 W/cm^2 for 5 min, $p < 0.01$. (b) Comparison of therapeutic efficiencies of treatments by chemotherapy, photothermal therapy, additive chemotherapy and photothermal therapy, and synergetic chemotherapy and photothermal therapy, using FMP-CNSs as PTX carrier. (c) Biodistributions of FMP-CNSs in different organs and tissues of nude mice determined at 24 h to 96 h post-injection, $p < 0.01$. (d) NIR image of heart, kidney, liver, lung and spleen from FMP-CNSs (left) and PBS (right) treated mice at 96 h post-injection using an excitation wavelength of 745 nm. (e) H&E stained tissue sections of mouse heart, kidney, liver, lung and spleen obtained from mice receiving no injection and those injected with FMP-CNSs at a concentration of 1 mg mL^{-1}. The scale bar = 125 μm.

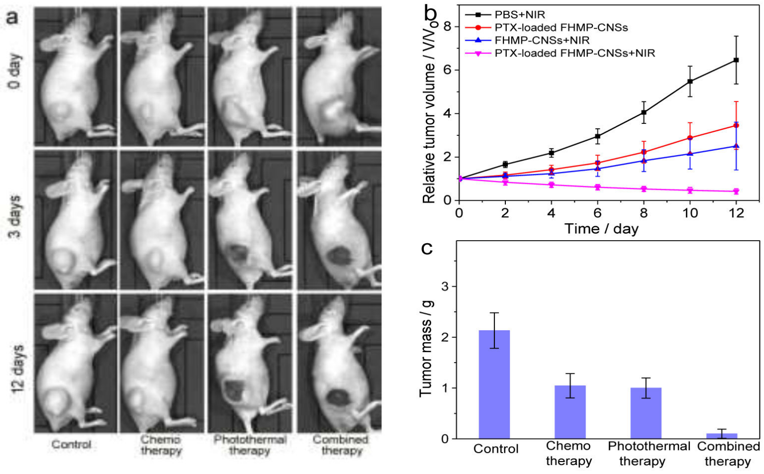

Fig. 5.

In vivo therapy of FMP-CNSs and PTX-loaded FMP-CNSs. (a) Photographs of tumors in mice treated under different conditions and imaged at pre-defined time points. (b) The tumor growth curves of mice treated under different conditions (four mice per treatment group). (c) Average weights of tumors harvested from mice at the end of treatments (day 7). (d) H&E-stained tumor sections collected from mice after treatments (scale bar = 125 μm).